Core–shell structure of carbon nanohorns and pH-sensitive liposome for active ingredient and tumor-associated macrophage polarization factor interleukin-21 codelivery

Xiao-Xue Zhang [a], Ge Tong [a], Dan Shen [a], Xue-Cheng Li [a], Li-Jing Lan [a], Xin Liu [a], Jing-Hao Cui [a], Renyu Huang [b,**], Beom-Jin Lee [c], Hong Gao [d], Qing-Ri Cao [a,*]

[a] College of Pharmaceutical Sciences, Soochow University, Suzhou, 215123, People's Republic of China
[b] College of Social Science, Institute of Culture and Tourism Development, Soochow University, Suzhou, 215123, People's Republic of China
[c] College of Pharmacy, Ajou University, Suwon, 16499, Republic of Korea
[d] PharmaMax Pharmaceuticals, Ltd., China Medical City, Taizhou, 225300, People's Republic of China

ARTICLE INFO

ABSTRACT

The combination of immunotherapy and chemotherapy is becoming a very promising cancer treatment method. However, the effective delivery of chemical drug or immune molecule to targeting tissues is a scientific issue to be solved urgently. A novel core–shell structure of single-walled carbon nanohorns (SWCNHs) and pH-sensitive liposome (PSL) was constructed for active ingredient (DOX) and tumor-associated macrophage (TAM) polarization factor interleukin-21 (IL-21) codelivery in this study. The physicochemical properties, cytotoxicity, cellular uptake, macrophage polarization, and antitumor efficacy of functionalized nanocarriers were fully evaluated. DOX was incorporated into oxidized SWCNHs via π–π interaction (DOX-O-SWCNH) and then coated with IL-21- loaded PSL to obtain IL-21-loaded PSL (IL-21-PSL)-DOX-O-SWCNHs. The release rates of IL-21 and DOX from functionalized nanocarriers at the pH 7.4 of were lower than those at the pH of 5.5, thereby indicating a pH- sensitive drug release. Blank nanocarriers showed relatively low cytotoxicity to A549 cells and 293T cells. The half maximal inhibitory concentration (IC50) value of PSL-DOX-O-SWCNHs for A549 cells was 164.85 μg/ mL. The PSL-DOX-O-SWCNHs can be effectively uptaken by A549 cells and the IL-21-PSL-DOX-O-SWCNHs can significantly downregulate the expression of M2 macrophage-related factors (IL-10 levels) and upregulate that of M1 macrophage-related factors (iNOs levels). The IL-21-PSL-DOX-O-SWCNHs also showed significantly high tumor targeting and distribution and significantly low tumor volume of A549 lung cancer cell-bearing nude mice, showing the cooperating effects of DOX and IL-21. The functionalized nanocarriers were mainly distributed in the tumor tissues and liver and less in the spleen, lung, and heart of mice. In conclusion, the functionalized IL-21- PSL-DOX-O-SWCNHs showed high drug loading, excellent cellular uptake, pH-sensitive release, TAM polariza-tion, and remarkable antitumor efficacy in vivo.

1. Introduction

Cancer will become the leading cause of death in every country in the 21st century [1,2]. Chemotherapeutics, also known as cytotoxic drugs, have been used in antitumor therapy since the 1940s. They played an important role in tumor treatment [3,4]. However, conventional chemotherapy with a single drug often results in serious side effects in prolonged treatment periods [5]. Therefore, combination, synergistic chemotherapy is a common strategy, and has been recommended for

tumor treatment due to its promoted therapeutic effect and reduced systemic toxicity [6–8]. Immunotherapy is increasingly used for cancer treatment and can be synergistic with chemotherapy [9,10]. It may involve diverse treatments, ranging from use of tumor vaccines, TLR agonists, cytokines, and agents that counter of immunosuppression, including checkpoint inhibitors [11,12]. With immunotherapy and chemotherapy strategically combined, cancer patients have a great possibility to overcome the difficulties of immunotherapy due to the utilization of potential synergies [13]. In particular, the therapy through

Table 1
Relevant primers used in the real-time qPCR study.

iNOs forward	GAACTGTAGCACAGCACAGGAAAT
iNOs reverse	CGTACCGGATGAGCTGTGAAT
IL-10 forward	ACCTGGTAGAAGTGATGCC
IL-10 reverse	CAAGGAGTTGTTTCCGTTA
IL-12p35 forward	ACGCAGCACTTCAGAATCAC
IL-12p35 reverse	CGCAGAGTCTCGCCATTATG
TGF-β forward	CAACAATTCCTGGCGTTACCT
TGF-β reverse	TGTATTCCGTCTCCTTGGTTCA
β-actin forward	GCACCACACCTTCTACAA
β-actin reverse	TACGACCAGAGGCATACA

targeting different elements of tumor biology, a prospective cancer treatment strategy, aims to exert synergistic anticancer effects [14–16].

The growth of neoplastic tissues can be effectively inhibited by human immune system, which is capable of recognizing and destroying transformed cells [17]. Served as one of these neoplastic cells, macrophages are so flexible that can change their phenotypes speedily in reply to their local signals. Once macrophages enter the typical (M1) activation state under the exposure to bacterial products and Th1 cytokines, their inflammatory activity, tumor killing function and T cell response can be promoted. Macrophages often go through alternative(M2) activation in reply to Th2 cytokines. At this time, supporting tumor growth, interfering antitumor immunity and promoting tissue repair are their functions [18–20]. In malignant tumors, M2-type tumor-associated macrophages (TAMs) are a hopeful target for tumor therapy. The most potent antitumor strategy should distort M2-type TAMs to M1-type macrophages [21]. Effect delivery of IL-21 to tumor tissue can cause TAM polarization from the M2 to the M1 phenotype, further leading to antitumor effect and tumor regression activated by T cell responses [22].

However, the effective systemic delivery of the immune cytokine together with a chemical compound to the tumor site is a core issue to be solved promptly.

Single-walled carbon nanohorns (SWCNHs) are small graphene sheets that are enfolded to form horn-type cones with a length of 30–50 nm and a diameter of 2–5 nm diameter [23]. After SWCNHs construction in gas phase, they are aggregated together to form similar to 'dahlia' flowers with a diameter of 100 nm [24]. SWCNHs can easily penetrate through the vasculature and accumulate in tumor sites by the EPR effect. In contrast to single-walled carbon nanotubes (SWCNTs), an advantage of SWCNHs is the lack of metal contamination [25,26]. In previous studies on the oxidation of SWCNTs, strong acids such as H_2SO_4 and HNO_3, have generally been used. But the reaction with these acids is difficult to control, thereby resulting in the formation of unwanted coalescence. In contrast with strong acids, H_2O_2 is advantageous in controlling the oxidation degree of SWCNHs [27,28]. SWCNH applications are related to their morphology and structure that are capable to store molecules into the inner space, thereby expecting the possible use as chemical drug carriers [29,30].

Liposomes have been commonly used for mediating the intracellular delivery of various biological molecules [31]. pH-sensitive liposomes (PSLs) are stable at normal physiological condition of pH 7.4, but destabilize under acidic tumor tissues, thereby releasing active compounds [32]. Different types of PSLs have been designed by the mechanism of striking pH sensitivity in the literature. Liposomes composed of dioleoyl phosphoethanolamine (DOPE) and cholesteryl hemisuccinate (CHEMS)/or phosphatidyl choline, or phosphatidylserine, or phosphatidylglycerol, have been incubated under overly acidic conditions [33–35]. Among these compositions, DOPE/CHEMS liposomes showed the highest pH sensitivity. At low pH of 5, the release of active
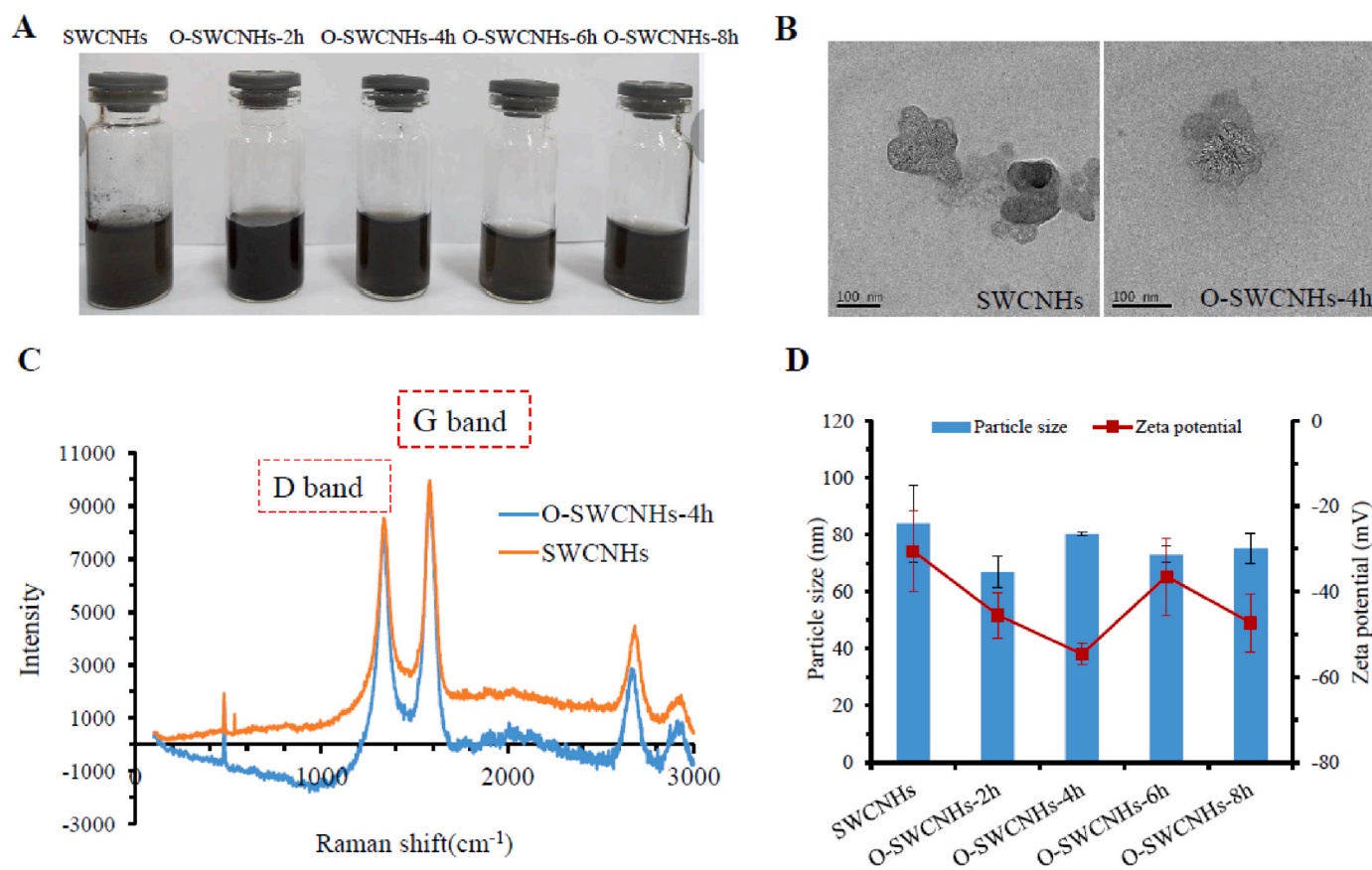
Fig. 1. Characterization of raw and oxidized SWCNHs. (A) Images of raw SWCNHs and O-SWCNHs oxidized for 2, 4, 6, and 8 h. (B) TEM images of raw SWCNHs and O-SWCNHs oxidized for 4 h. (C) Raman spectra of raw SWCNHs and O-SWCNHs for 4 h. (D) Particle size and Zeta potential of raw SWCNHs and O-SWCNHs oxidized for 2, 4, 6, and 8 h. All data are represented as mean ± SD (n = 3).
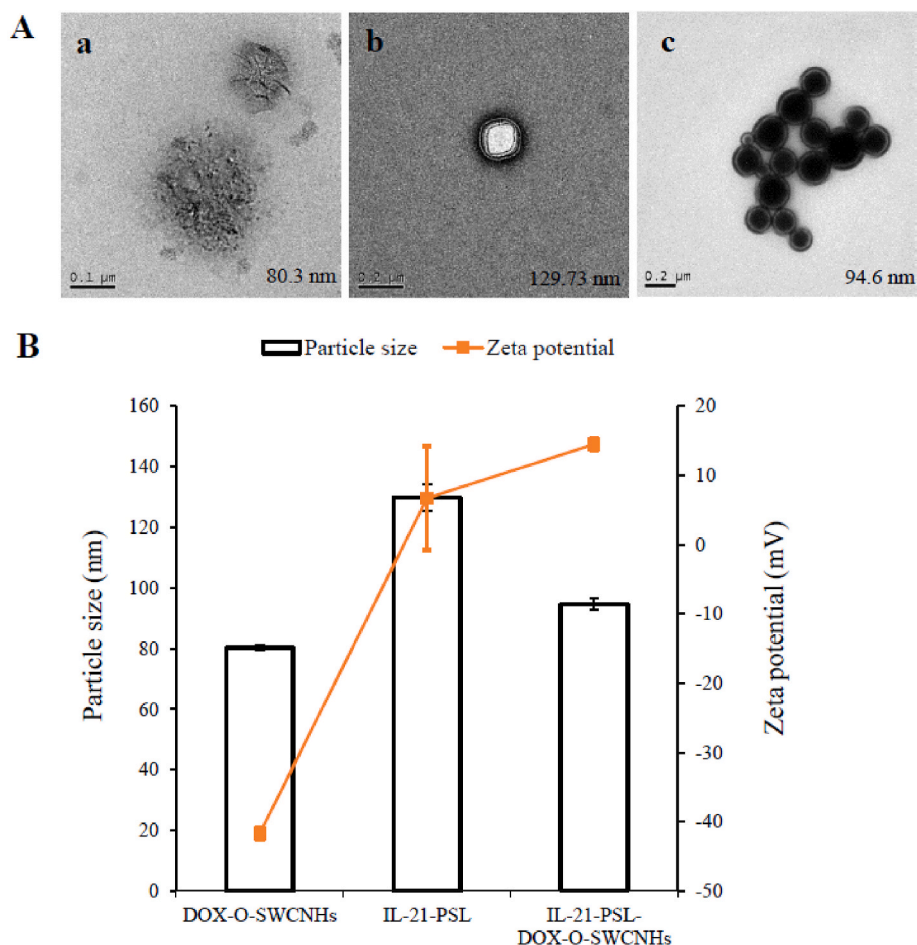
Fig. 2. PSL-coated SWCNH characterization. (A) Particle size and Zeta potential of O-SWCNHs, PSL, and PSL-O-SWCNHs. All data are represented as mean ± SD (n = 3). (B) TEM images of O-SWCNHs (a), PSL(b), and PSL-O-SWCNHs (c).

component and lipid intermixing was observed with DOPE/CHEMS liposomes [36].

In this study, to achieve the effective delivery of chemical drug (poorly water soluble) and immune molecule (highly water soluble) to targeting tumor tissues, we constructed a novel core–shell structure of SWCNHs and pH-sensitive PSL composed of DOPE and CHEMS for active ingredient (DOX) and TAM polarization factor interleukin-21 (IL-21) codelivery. The physicochemical properties, cytotoxicity, cellular up-take, macrophage polarization, and antitumor efficacy of functionalized nanocarriers were fully evaluated. The initial core–shell structure of nanocarrier can be maintained during systemic circulation, but PSL was destroyed by the acidic pH of tumor tissues, followed by the release of IL-21 for the polarization of TAMs. Meanwhile, the isolated core composed of DOX-O-SWCNHs can also facilitate the release of drug at low pH, thereby resulting in the synergistic effect of DOX and IL-21.

2. Materials and methods

2.1. Materials

Active Ingredient hydrochloride (DOX·HCl, purity ≥99%) was purchased from Suzhou argon krypton xenon trade Co., Ltd. (Suzhou, China). Single-walled carbon nanohorns (SWCNHs, purity ≥89%) were pur-chased from Suzhou Universal Group. (Suzhou, China). Hydrogen peroxide 30% was provided by NanJing KeyGen Biotech (Nanjing, China). Lipoid DOPE was purchased from Lipoid GmbH (Ludwigshafen, Germany). DMEM medium with fetal bovine serum (FBS) and high glucose were purchased from Hyclone (Logan, USA). Cholesteryl

hemisuccinate (CHEMS), coumarin 6, acetonitrile and methanol (HPLC grades) were supported by Sigma-Aldrich (Darmstadt, Germany). WST-1 Assay reagent-cell proliferation and Hoechest33342 were provided by BIB (Haimen, China). Cy5.5-NS was supported by *Lumiprobe* (USA). Ultrafiltration centrifuge tubes (Amicon®Ultra 3K & 100K) were pur-chased from Merck (Darmstadt, Germany). Dialysis bag 3500 was pur-chased from Shanghai YuanYe Biological (Shanghai, China).

2.2. Methods

2.2.1. Preparation of the functionalized SWCNHs

2.2.1.1. Preparation of O-SWCNHs.
O-SWCNTs were prepared through treatment with an oxidizing agent. In contrast with strong acids, H_2O_2 as an oxidizing agent is advantageous in modulating the oxidation degree [27,37]. Briefly, 50 mg raw SWCNHs were dispersed in 50 mL of H_2O_2. Then, dispersal was refluxed under agitation in an oil bath (75 °C) for 2, 4, 6, and 8 h to compare the effect of time on the different surface oxidation degrees. The suspension was cooled to room temperature and kept for 30 min. After removing the acidic supernatant, the precipitate was then diluted with distilled water. The obtained suspension was filtered through 0.22 μm cellulose membrane and rinsed with excess deionized water to neutralize the pH of the filtrate. The product was dried in a vacuum dryer at 40 °C for 1 h to acquire the O-SWCNHs.

2.2.1.2. Synthesis of DOX-O-SWCNHs.
DOX and O-SWCNHs with a drug/carrier ratio of 1:4 (w/w) were suspended in phosphate-buffered saline (PBS, pH 7.4). The resulting mixture was sonicated at 400 W for
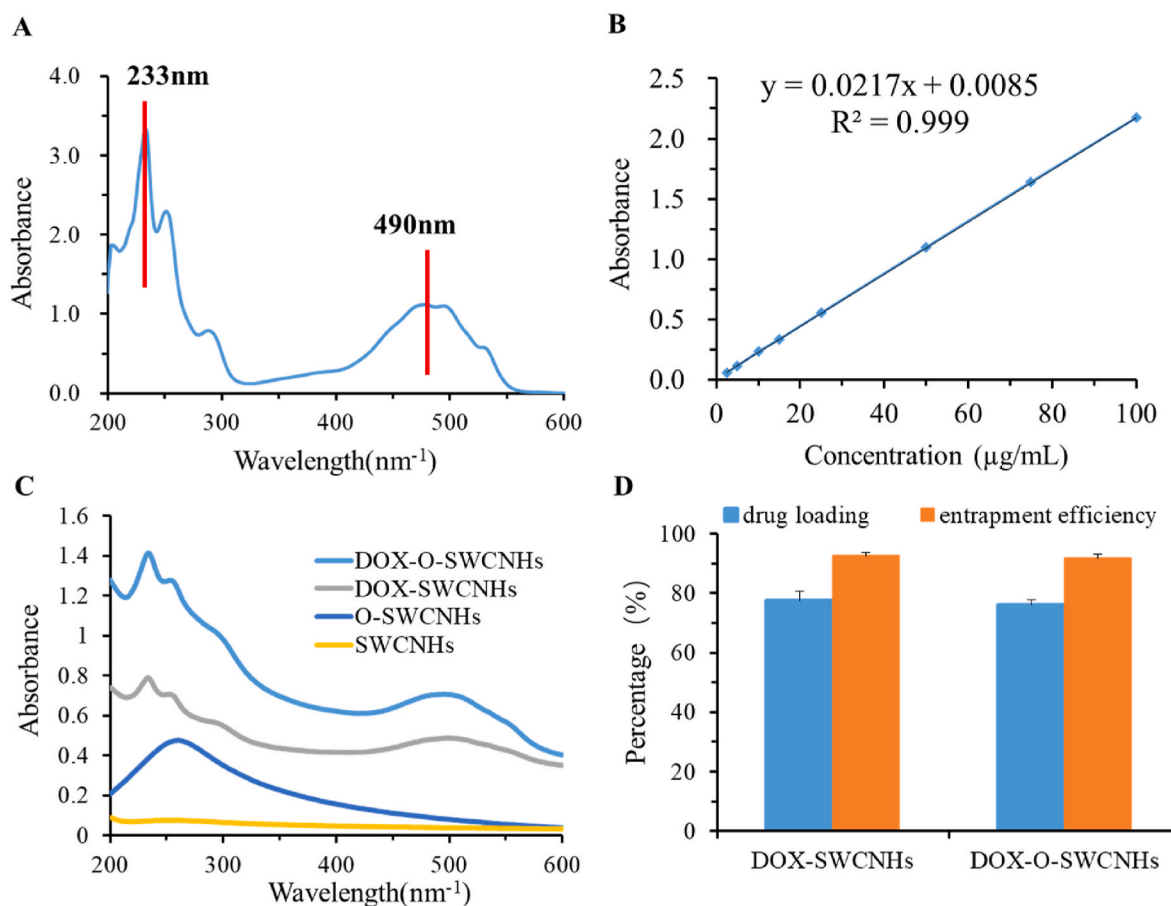
Fig. 3. Drug loading and encapsulation efficiencies of drug-loaded SWCNHs. (A) UV–vis spectrum of DOX. (B) Calibration curve of DOX. (C) UV–vis spectrum of SWCNHs, O-SWCNHs, DOX-SWCNHs, and DOX-O-SWCNHs. (D) Drug loading and encapsulation efficiencies of DOX-SWCNHs and DOX-O-SWCNHs (n = 3).

30 min by using an ultrasonic grinder. The reaction of the mixture was then performed overnight under consecutive stirring, followed by centrifugation at 10,000 rpm for 10 min. The solid mass was redispersed in PBS after removing the supernatant, and then centrifuged again under the same condition. The sedimentation was washed five times independently using PBS (pH 7.4) to remove free DOX, and then dried at 40 °C to get DOX-O-SWCNHs. The carrier/drug ratio and preparation conditions were optimized by determining the drug-loading rate of O-SWCNHs.

2.2.2. Preparation of IL-21-PSL
Blank PSL was prepared via reverse evaporation. The DOPE and CHEMS (3:1, 4 mg in total) were dissolved in 1 mL of organic solvent (methanol: chloroform = 1:2). Then, 5 mL of phosphate buffer was added into the organic solution. The solvent was evaporated in a rotary evaporator in a 50 °C bath under reduced pressure. The resulting liposomes were extruded through a 200 nm membrane using a HandExtruder (Genizer™-1ml) to reduce their particle size [38,39].

The IL-21 solution was added to the blank PSL at an IL-21/lipid ratio of 1:30 (w/w), and then the mixture was stirred for 6 h at 25 °C. Free IL-21 was separated from the IL-21-PSL by using ultrafiltration centrifuge tubes (100 K) to obtain IL-21-loaded pH-sensitive liposomes.

2.2.3. Preparation of IL-21-PSL-DOX-O-SWCNH
DOX-O-SWCNHs were dispersed in PBS to form a 0.2 mg/mL of suspension. DOX-O-SWNHs and IL-21-PSL at a volume ratio of 1:1 was mixed and thoroughly sonicated to obtain IL-21-PSL-DOX-SWCNHs.

2.2.4. Characterization of the functionalized SWCNHs

2.2.4.1. Dispersibility.
SWCNHs and O-SWCNHs oxidized for different times were dissolved in 2 mL of PBS (pH of 7.4). The resulting mixture was sonicated using an ultrasonic grinder for 10 min and allowed to maintain for 24 h.

2.2.4.2. Evaluation of the surface morphology.
The images of SWCNHs, O-SWCNHs, DOX-O-SWCNHs, IL-21-PSL, and IL-21-PSL-DOX-O-SWCNHs were acquired by transmission electron microscopy (FEI Tecnai G20, USA).

2.2.4.3. Raman spectroscopy.
The intensity ratio of G-band to D-band (I_G/I_D) accounted for the structural characterization of SWCNHs. The Raman spectra of SWCNHs and O-SWCNHs were recorded on a Fourier transform spectrophotometer (Brüker RFS 100) with a power of 50 mV at a wavelength of 1064 nm.

2.2.4.4. Determination of the zeta potential and particle size.
The zeta potential and average diameter of the functionalized SWCNHs dispersed in PBS (pH of 7.4) were measured using Zeta Sizer Nano Series (NICOMP 380ZLS).

2.2.4.5. Determination of the encapsulation efficiency and drug loading.
To confirm the maximum absorption wavelengths of DOX, we measured the absorption of 100 µg/mL DOX at a wavelength of 200–600 nm in an ultraviolet–visible spectrophotometer (Kyoto, Japan). A series of concentrations of DOX was also measured at 490 nm to draw a calibration curve. To verify the drug loading, we independently suspended the

A

B
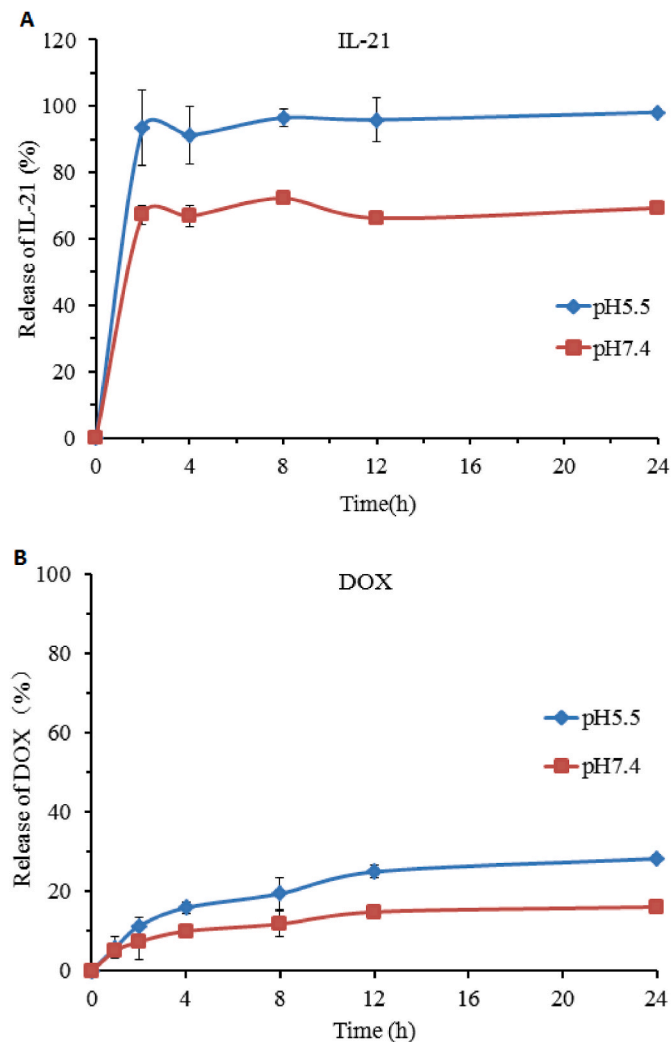
Fig. 4. Accumulative release profiles of DOX and IL-21 from IL-21-PSL-DOX-O-SWCNHs. (A) IL-21. (B) DOX.

SWCNHs, O-SWCNHs, DOX-SWCNHs, and DOX-O-SWCNHs in water. The spectra of the samples were checked at a wavelength of 200–600 nm. The encapsulation efficiency of DOX-O-SWCNHs was determined by checking DOX concentration in the supernatant. The drug loading and encapsulation efficiency was estimated from the following equations.

$$\text{SWCHN drug loading } (\%) = \frac{W_{DOX}}{W_{carrier} + W_{DOX}} \times 100\%$$

$$\text{SWCNH encapsulation efficiency } (\%) = \frac{W_{totalDOX} - W_{freeDOX}}{W_{totalDOX}} \times 100\%$$

Meanwhile, the encapsulated efficiency of IL-21 in IL-21-PSL-DOX-SWCNHs was calculated by determining the free IL-21 by using a fluorescence spectrophotometer. The DOX and IL-21 loadings of IL-21-PSL-DOX-SWCNHs were calculated based on the mass ratio of IL-21: DOPE: CHEMS: DOX-O-SWCNHs (1:30:10:20).

DOX loading of $IL - 21 - PSL - DOX - O - SWCNHs$ (%)

$$= \frac{W_{DOX-O-SWCNHs} * W_{DOX}\%}{W_{IL-21} + W_{PSL} + W_{DOX-O-SWCNHs}} \times 100\%,$$

$IL - 21$ loading of $IL - 21 - PSL - DOX - O - SWCNHs$ (%)

$$= \frac{W_{IL-21} * W_{IL-21}\%}{W_{IL-21} + W_{PSL} + W_{DOX-O-SWCNHs}} \times 100\%,$$

where W_{DOX} % indicates the DOX loading of DOX-O-SWCNHs, and W_{IL-21}% indicates the IL-21 loading of IL-21-PSL.

2.2.4.6. In vitro IL-21 and DOX release. DOX, DOX-SWCNHs, and DOX-O-SWCNHs were dispersed in PBS solution (pH of 5.5 or 7.4) and filled into a dialysis bag, which was then immersed in PBS as dissolution medium. The dissolution apparatus was placed in a water bath (37 °C) and shaken at 100 rpm. At scheduled time intervals (1, 2, 4, 8, 12, and 24 h), the release sample was withdrawn, and then a fresh PBS was added to maintain the sink condition. The release percentage of DOX was calculated by determining the absorbance of sample at 490 nm.

Cy5.5-IL-21-PSL-DOX-O-SWCNHs was dispersed in PBS solution (pH of 5.5 or 7.4), and the suspension was treated as the method described above. At scheduled time intervals, the samples were withdrawn, followed by monitoring the fluorescence intensity using a fluorescence spectrophotometer. The emission and excitation wavelengths were 695 and 675 nm, respectively. DOX concentration was also determined by measuring the sample absorbance.

2.2.5. Cell culture and maintenance

Murine-derived RAW 264.7 macrophages were cultured in high-glucose DMEM supplemented with 1% active ingredient/active ingredient and 10% fetal bovine serum. Recombinant murine IL-4, IL-21 and LPS were provided by PeproTech (Rocky Hill, NJ).

2.2.5.1. Cytotoxicity. The cytotoxicities of blank SWCNHs to A549 and 293T cells were evaluated via WST-1 assay. The cell viabilities of blank SWCNHs on A549 and 293T cells were studied for four groups, including control, O-SWCNHs, PSL-SWCNHs, and PSL-O-SWCNHs. Briefly, A549 and 293T cells were seeded in 96-well plates at a density of 8×10^4 cells per well during logarithmic growth phase and cultured for 24 h at 37 °C in a humid environment containing 5% CO_2. After removal of the culture medium, the test samples were incubated for 24 or 48 h with the addi-tion of negative controls and fresh medium dilutions. Each group sets up six parallel samples. Afterward, the cells were rinsed twice with PBS. 90 μL of medium and 10 μL of WST-1 (5 mg/mL) were added to each well and stained for 2 h at 37 °C. The plate was shaken by an oscillator, and absorbance was determined at 630 nm. The cell viability of blank SWCHNs was calculated using the following equation:

Cell viability (%) = (A630experiment – A450blank)
/ (A630control – A450blank) × 100%.

The cell viability of drug-loaded SWCNHs on A549 cells was also evaluated by WST-1 assay. A549 cells were planted in 96-well plates at a density of 8×10^4 cells per well during the logarithmic growth phase, and the cells were then incubated for 24 h at 37 °C in a humid envi-ronment containing 5% CO_2. Following the removal of the culture media, various concentrations of PSL-DOX-O-SWCNHs were added along with fresh medium and cultured for 24 h. Subsequently, the cell viability was determined for the calculation of IC50 value.

2.2.5.2. Cellular uptake and intercellular localization. At a density of 2×10^5 cells/well, A549 cells in the logarithmic phase were seeded in 6-well plates and incubated for 24 h. Following the removal of the medium, 2 mL of DOX-O-SWCNHs or PSL-DOX-O-SWCNHs (50 μg/mL) were added to the cells, and then incubated for 2 h. The treated cells underwent triple PBS washes, an addition of 0.25% trypsin, and a centrifugation for 5 min at 1,000 rpm. The collected cells were rinsed twice more with PBS and analyzed in terms of the cellular uptake of functionalized SWCNHs by a flow cytometry (FACSCalibur, Becton Dickinson, USA).

Coumarin-6-labeled PSL-DOX-O-SWCNHs or DOX-O-SWCNHs (50 μg/mL) was added to A549 cells and then the endocytosis mechanism of functionalized SWCNHs was evaluated at 2 h. The confocal laser scan-ning microscope was used to observe the resulting cells stained with Hoechst33342.
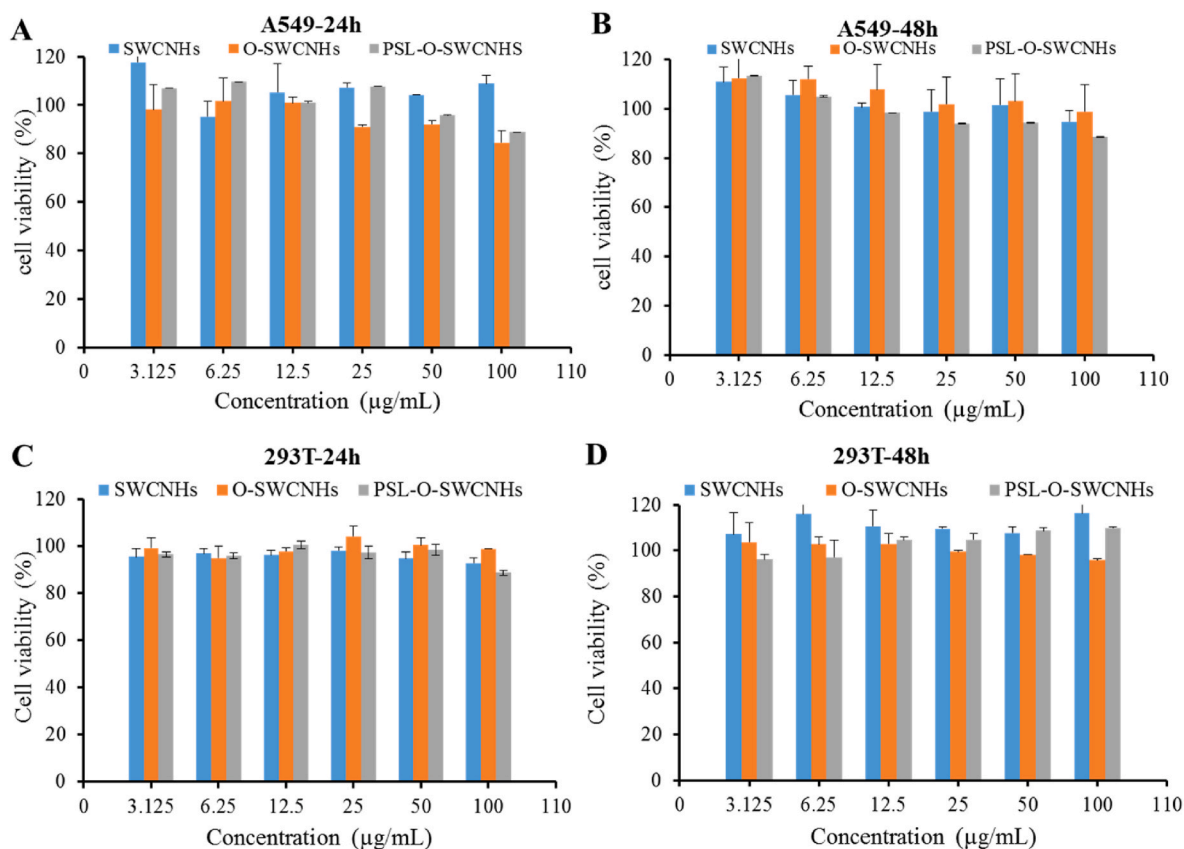
Fig. 5. Cell viability of A549 and 293T cells incubated with functionalized SWCNHs for 24 and 48 h. (A) A549-24 h. (B) A549-48 h. (C) 293T-24 h. (D) 293T-48 h.
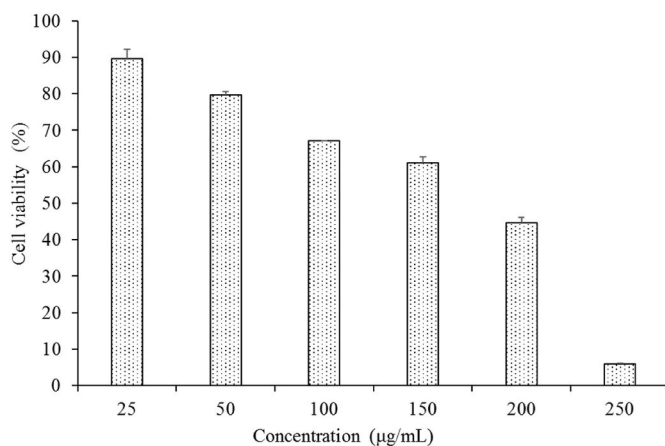
Fig. 6. Cell viability of PSL-DOX-O-SWCNHs in A549 cells at 24 h.

2.2.6. Macrophage polarization

Real-time quantitative PCR (qPCR) was used for all mRNA analyses. Briefly, total RNA from cultured or sorted cells was extracted using the RNeasy Kit (QIAGEN) according to the manufacturer's instructions. First-strand cDNA was synthetic and qPCR (Bio-Rad CFX96) was performed using SYBR Green qPCR SuperMix (TransGen) and the relevant primers. According to $\Delta\Delta$Ct method, gene expression was normalized to β-actin. Primers used in this study are listed in Table 1.

2.2.6.1. Macrophage induction. At a density of 6×10^4 cells per well, RAW 264.7 cells were seeded in a 6-well plate, followed by incubating for 24 h. After treatment with medium containing 25 ng/mL IL-4 or 100 ng/mL lipopolysaccharide (LPS) for 24 h, the cells were washed with

PBS solution. The expression level of primers was analyzed after RNA was extracted.

2.2.6.2. IL-21 shifting macrophages from M2 to M1. At a density of 6×10^4 cells per well, RAW 264.7 cells were seeded in a 6-well plate, followed by incubation for 24 h. Then, cells treated with 25 ng/mL IL-4 were cultured for 24 h. After treatment with the medium containing 12.5, 25, and 50 ng/mL IL-21 for 24 h, the cells were washed with PBS solution. The expression level of primers was analyzed after RNA was extracted.

2.2.6.3. IL-21-PSL-O-SWCNHs shifting macrophages from M2 to M1. At a density of 6×10^4 cells per well, RAW 264.7 cells were seeded in a 6-well plate. After incubation for 24 h, the cells were treated with 25 ng/mL IL-4. After culturing for 24 h, 2 mL of medium containing IL-21-PSL-O-SWCNHs (150 μg/mL) was used in the replacement of the culture medium.

The culture medium was removed after treatment for 24 h, and the PBS solution was used for washing cells. The expression level of primers was analyzed after RNA was extracted.

2.2.7. Animal study

2.2.7.1. Cy5.5-labeled IL-21 preparation. IL-21 was labeled with Cy5.5 through amide bond. A total of 1 mg/mL of IL-21 (10 μL) were dispersed in 1 mL of PBS (pH of 7.4) and then mixed with 10 mL of Cy5.5 (1 mg/mL). The resulting suspension was magnetically stirred overnight and further centrifuged in ultrafiltration centrifuge tubes (3 K) at 10,000 rpm for 10 min.

2.2.7.2. Tumor-bearing mouse model establishment. Female nude mice (BALB/c, 3–4 weeks old) were kept separately under SPF conditions and
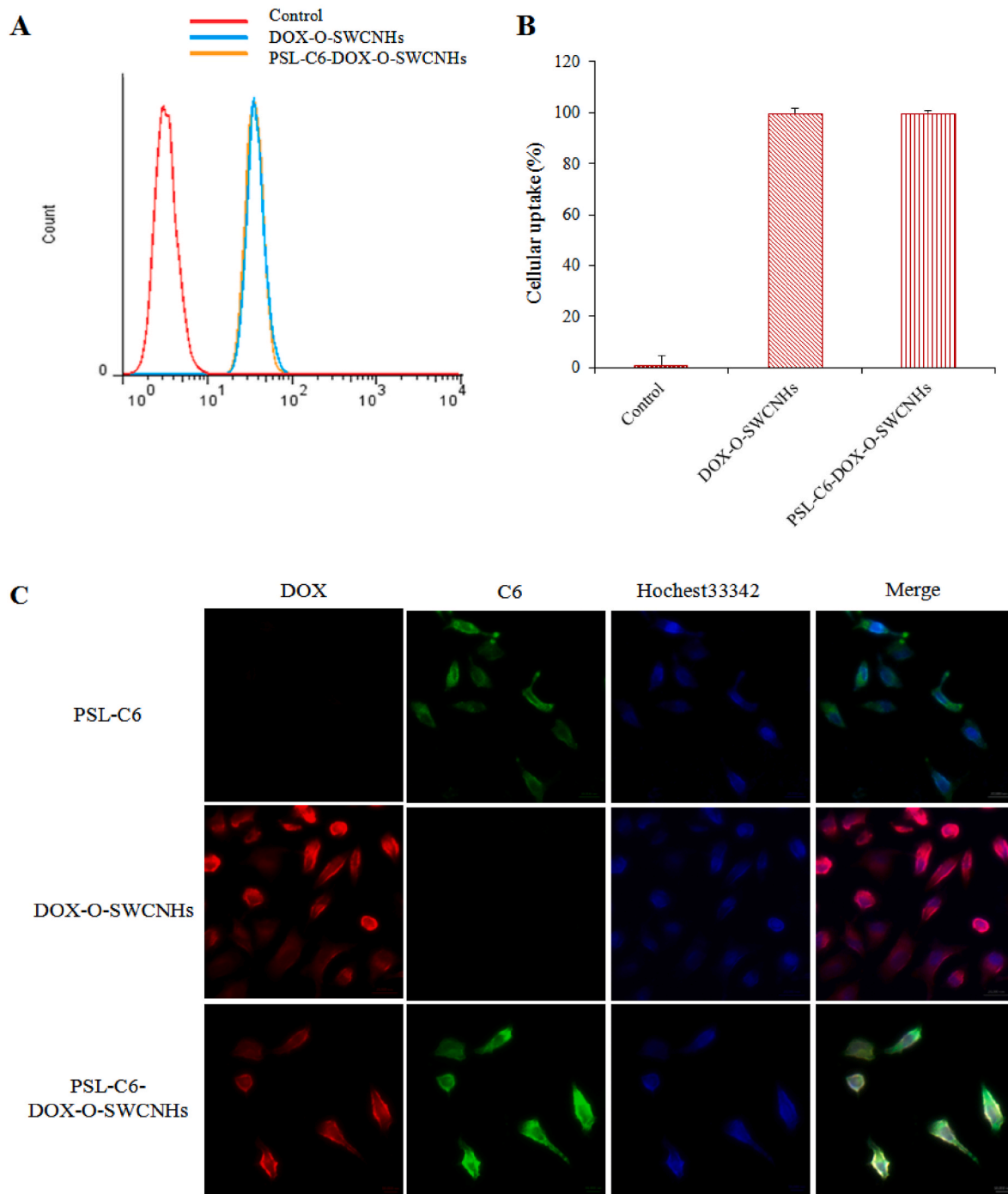
Fig. 7. Cellular uptake of functionalized SWCNHs in A549 cells. (A) Cellular uptake of control, DOX-O-SWCNHs, and PSL-C6-DOX-O-SWCNHs groups determined by flow cytometry. (B) Quantitative analysis of cellular uptake. (C) Fluorescent images of PSL-C6, DOX-O-SWCNHs, and PSL-C6-DOX-O-SWCNHs detected by CLSM.

had unrestricted access to sterilized food. The mice were given non-small lung cancer A549 cells during the logarithmic growth phase at a concentration of 1×10^7 cells/mL in PBS after adapting to breeding conditions for 1 week. One hundred microliter of the cell suspension was injected subcutaneously into the peritoneal cavity of nude mice and kept under SPF environment.

2.2.7.3. Tumor-targeting ability. Six tumor-bearing nude mice were separated into two groups randomly and injected intravenously with Cy5.5-IL-21-PSL-DOX-O-SWCNHs and Cy5.5-IL-21 at the dose of 0.2 mL via the tail vein. Each group has three mice which were anesthetized

with active ingredient at various time intervals, followed by 5 days of real-time in vivo fluorescence imaging using a small animal imager (Caliper IVIS Lumina II, USA) at an excitation wavelength of 675 nm and an emission wavelength of 695 nm. The mice in each group were also killed after 48 h. Heart, liver, spleen, lung, kidney and tumor tissues were taken to assess the tissue distribution of functionalized SWCNHs. Each organ was rinsed with physiological saline and imaged by fluorescence scanning.

2.2.7.4. In vivo antitumor effects. Within 2–3 weeks after non-small lung cancer A549 cell implantation, subcutaneous tumors formed. The experiment can begin as soon as the tumor reaches a size of 50–80 mm^3.
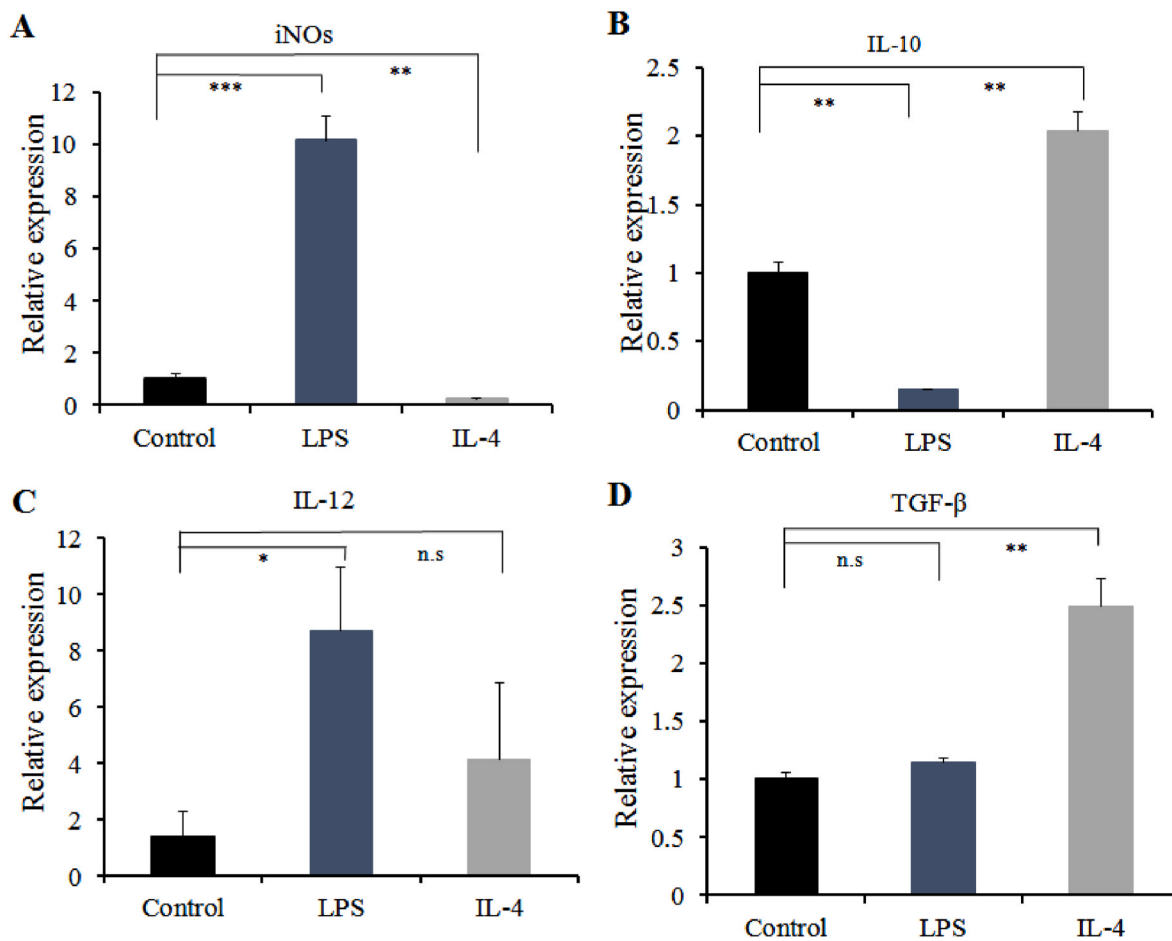
Fig. 8. Cytokine levels of macrophage treated with LPS and IL-4. (A) iNOs. (B) IL-10. (C) IL-12. (D) TGF-β. *p < 0.05, **p < 0.01, ***p < 0.001; n.s., not significant.
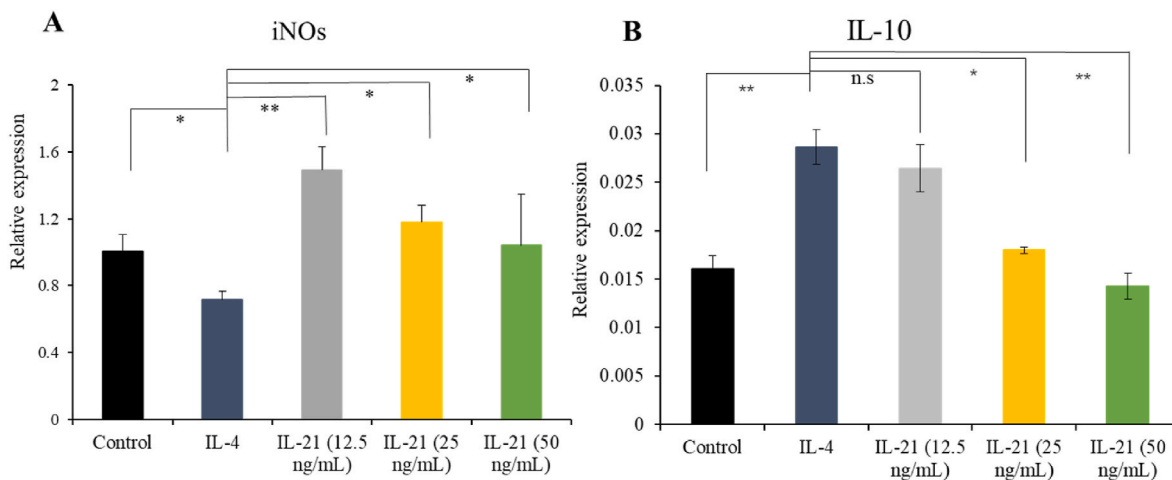
Fig. 9. Cytokine levels of macrophage treated with polarization factor IL-21. (A) iNOs. (B) IL-10. *p < 0.05, **p < 0.01, and ***p < 0.001; n.s., not significant.

The following four groups of twenty-four tumor-bearing nude mice were created at random: physiological saline (NS control group), IL-21-PSL, PSL-DOX-O-SWCNHs, and IL-21-PSL-DOX-O-SWCNHs. At 2-day intervals, through the tail vein, these groups of mice were injected with five doses of various formulations amounting to 5 mg/kg of DOX. Equal volumes of saline were given to the control and drug groups. The mice were weighed regularly during the experiment, and tumor sizes were determined every two days using calipers. $V = a \times b^2 \times 0.5$ was used as the formula for calculating tumor volume. Relative tumor volume (RTV) was determined using the formula $RTV = V_d/V_o$, where V_d denotes the tumor volume following therapy and V_o denotes the tumor volume prior to treatment (d0). The tumor inhibition rate was assessed using the formula: (average tumor volume of control group−average tumor volume of treatment group)/average tumor volume of control group × 100%. Based on the data collected throughout the experiment, the changes in body weight and tumor size in nude mice were recorded as a function of time.
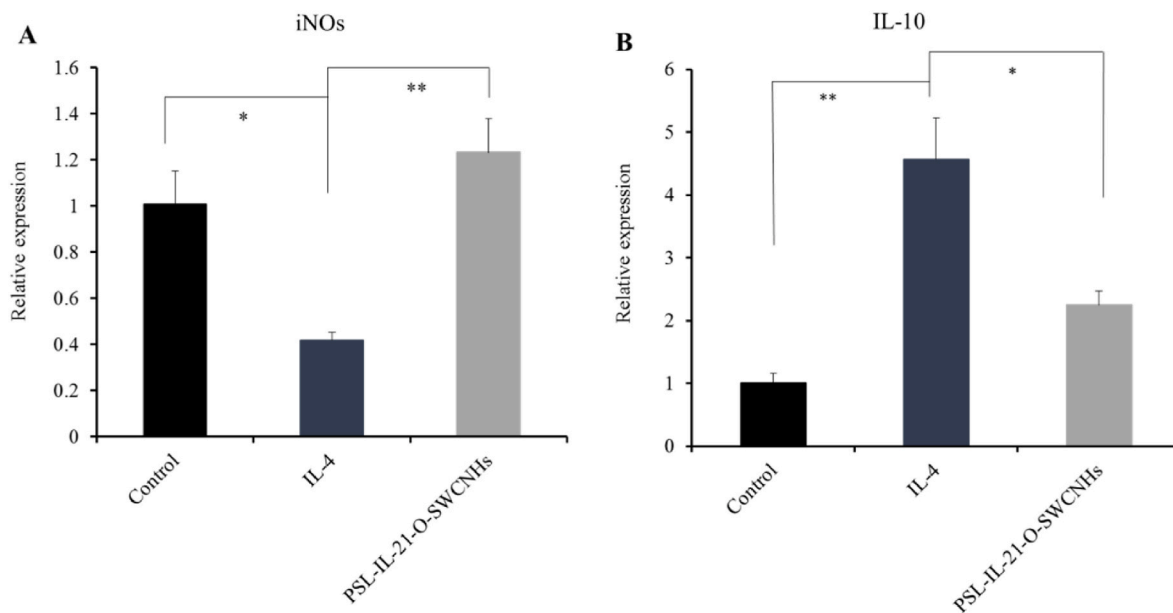
Fig. 10. Cytokine levels of macrophage treated with IL-21-PSL-O-SWCNHs. (A) iNOs. (B) IL-10. *p < 0.05, **p < 0.01, and ***p < 0.001; n.s., not significant.
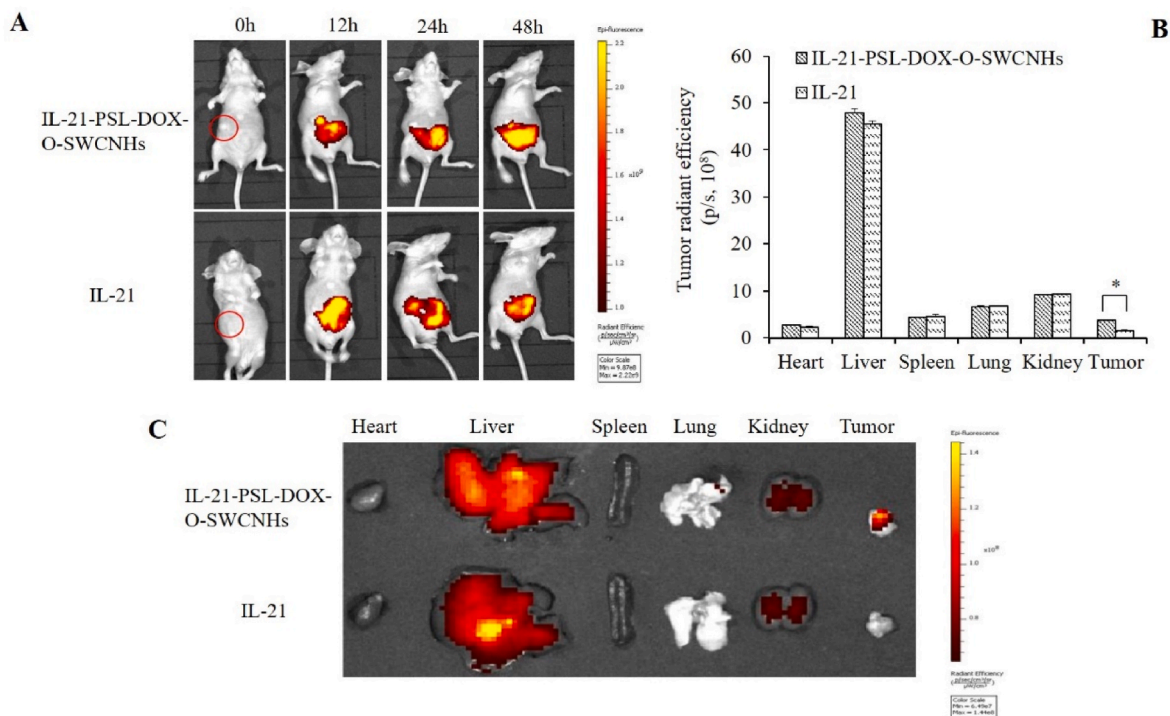
Fig. 11. (A) In vivo fluorescence images of A549 tumor-bearing nude mice after IL-21-PSL-DOX-O-SWCNH administration through tail vein. (B, C) Fluorescence images of various organs at 48 h after a single administration of IL-21-PSL-DOX-O-SWCNHs through the tail vein.

2.2.8. Statistical analysis

Data were presented as mean ± SD, and statistical significance was checked using the SPSS 13.0 software. Significant differences between different groups were evaluated by ANOVA. p < 0.05 was considered statistically significant (***p < 0.001, **p < 0.01,*p < 0.05).

3. Results and discussion

3.1. Characterization of the O-SWCNHs

As a mild oxidizing agent, H_2O_2 is useful in controlling the oxidation degree of SWCNHs. To evaluate the dispersibility of SWCNHs, we dispersed raw SWCNHs and O-SWCNHs oxidized for different periods in the PBS solution. A small amount of precipitation was formed for raw SWCNHs within 2 h. However, all the different O-SWCNHs were dispersed well in the solution even for several days (Fig. 1A). Oxidation
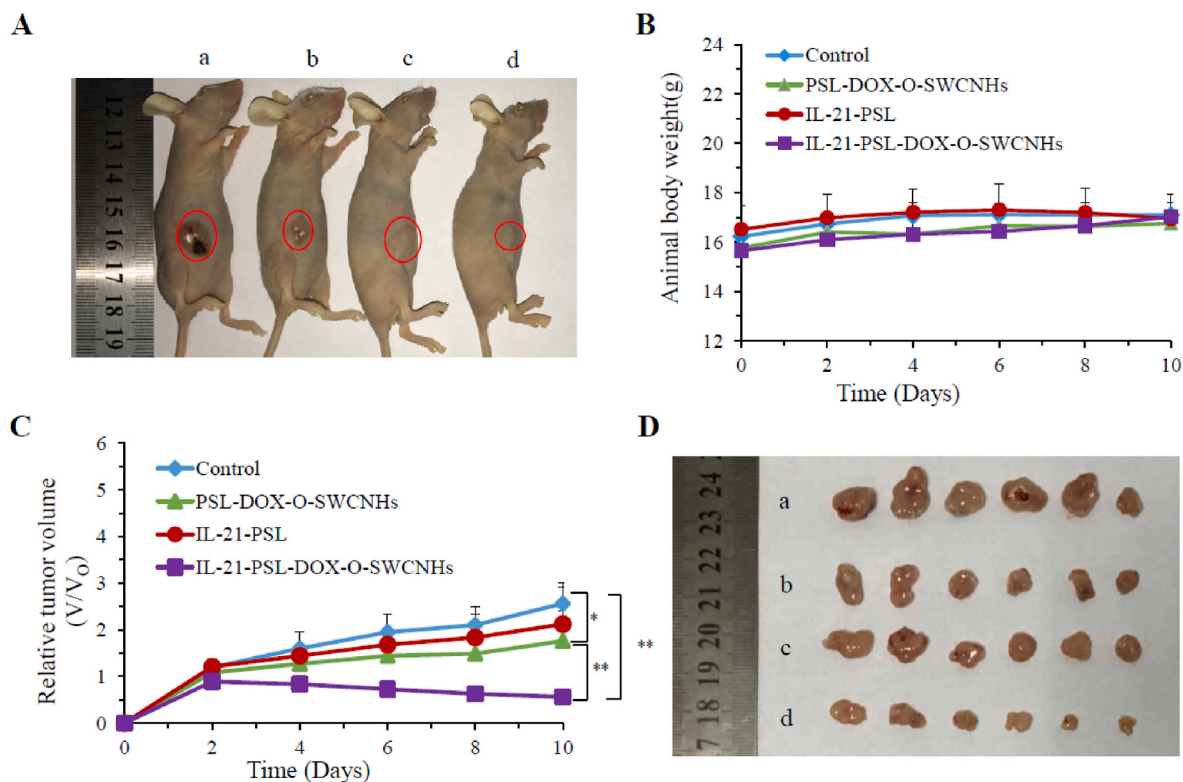
Fig. 12. (A) Image of tumor-bearing nude mice administered through tail vein after 10 days. (B) Changes in body weight. (C) Changes in relative tumor volumes. (D) Tumor volumes of mice administered through the tail vein after 10 days (a: control, b: PSL-DOX-O-SWCNHs, c: IL-21-PSL, d: IL-21-PSL-DOX-O-SWCNHs). All data are represented as mean $\pm$ SD (n = 6).

resulted in high dispersibility in aqueous medium due to the enhanced O-SWCNH hydrophilicity.

The electron microscopy was used to examine the morphological changes that occurred during the oxidation process. As shown in the TEM images (Fig. 1B), O-SWCNHs showed a regular hole-forming morphology after being oxidized for 4 h, while raw SWCNHs without treatment aggregated with each other, thereby forming an irregular morphology.

To verify the success of the oxidation process of carbon nanomaterial, Raman spectroscopy is performed in different modes. In Raman spectrum, G-mode accounts for the graphitic mode, which is associated with the double bonds between the carbon atoms (C=C). On the other hand, D-mode originates on the accounts of disorderliness in the SWCNHs, which is related to the typical conical-shape of SWCNHs. The G- and D-bands occur at approximately 1591 and 1317 cm^{-1}, respectively. The IG/ID ratio was 1.3, which governed the high purity and ordered nature of SWCNHs (Fig. 1C).

The particle size and zeta potential were analyzed to assess the changes of the functionalized SWCNHs. The particle size of SWCNHs and O-SWCNHs dispersed in PBS was in the range of 65–75 nm (Fig. 1D), thereby suggesting that the difference in size before and after oxidation was insignificant. The zeta potential of SWCNHs was approximately −30 mV. O-SWCNHs presented relatively higher zeta potential than raw SWCNHs, which may be due to the abundant carboxyl groups formed by oxidation.

As shown from the peaks in the FT-IR spectra at 1600 cm^{-1} (Fig. S1), oxygenated groups including acid anhydrides and/or carboxylic acids, were present in O-SWCNHs corresponding to C=O stretching vibrations [40]. The C=C and C–O stretching were conjugated with C=O groups and exhibited two broad peaks at 1560 and 1170 cm^{-1} in the spectrum, respectively [41].

3.2. Characterization of the functionalized SWCNHs

The particle size and morphology of DOX-O-SWCNHs, IL-21-PSL, and IL-21-PSL-DOX-O-SWCNHs were compared and is shown in Fig. 2. After drug loading, DOX-O-SWCNHs showed a spherical shape with dahlia flower structure (Fig. 2Aa). The IL-21-PSL showed a spherical structure with an empty hole (Fig. 2Ab). A district PSL layer can be observed on the surface of DOX-O-SWCNHs for IL-21-PSL-DOX-O-SWCNHs, thereby forming a core-shell structure of the carrier (Fig. 2Ac). The particle sizes and zeta potentials of DOX-O-SWCNHs, IL-21-PSL, and IL-21-PSL-DOX-O-SWCNHs are presented in Fig. 2B. The mean diameters of DOX-O-SWCNHs, IL-21-PSL, IL-21-PSL-DOX-O-SWCNHs were 80.3 $\pm$ 0.84, 129.7 $\pm$ 4.38, and 94.6 $\pm$ 1.98 nm, respectively. Particle size slightly increased when DOX-O-SWCNHs were coated with IL-21-PSL. The zeta potential of DOX-O-SWCNHs was approximately −40 mV, whereas that of IL-21-PSL was positive charge with several mV. The negative charge of DOX-O-SWCNHs was converted to positive charge when the surface was coated with positively charged IL-21-PSL. This finding suggested that the zeta potential of IL-21-PSL-DOX-O-SWCNHs was dependent on the surface charge of IL-21-PSL, which was beneficial for internalization with negatively charged cancer cells.

3.3. Encapsulation efficiency and drug loading

The UV absorption spectra of DOX, SWCNHs, O-SWCNHs, DOX-SWCNHs, and DOX-O-SWCNHs were recorded to verify their formation (Fig. 3A and C). DOX had characteristic absorption peaks at 233 and 490 nm as shown in Fig. 3A. DOX absorption showed good linearity at a concentration range up to 100 μg/mL (Fig. 3B). DOX-SWCNHs and DOX-O-SWCNHs had distinct absorption peaks of DOX at 490 nm, thereby indicating that DOX had been successfully adsorbed onto SWCNHs and O-SWCNHs. However, the absorption peaks of DOX cannot be observed in the spectra of SWCNHs and O-SWCNHs (Fig. 3C). As shown in Fig. 3D,

the drug loadings of DOX-SWCNHs and DOX-O-SWCNHs were 77.61% and 75.99%, respectively. Meanwhile, the encapsulation efficacy was >90% for DOX-SWCNHs and DOX-O-SWCNHs. DOX-SWCNHs was similar with DOX-O-SWCNHs in regard to the conjugation rate of DOX [38].

Meanwhile, after the analysis for IL-21-PSL-DOX-O-SWCNHs, the DOX loading and IL-21 loading capacities were 25.33% and 1.67%, respectively. The IL-21-loading capacity of IL-21-PSL was investigated using a fluorescence spectrophotometer. The encapsulated efficiency of IL-21 was almost 100%. The fluorescence intensity of free IL-21 from ultrafiltration centrifuge tubes cannot be detected.

3.4. In vitro release of IL-21 and DOX

The in vitro drug release from free DOX, DOX-SWCNHs, or DOX-O-SWCNHs are shown in Fig. S2. For all groups, the release of DOX at pH 5.5 was significantly faster than that at pH 7.4 in the PBS solution (Fig. S2 A, B, and C). The release of DOX from DOX-SWCNHs or DOX-O-SWCNHs was also much lower than that of free DOX, thereby indicating that the interactions between the drug and carriers retard the drug release. As predicted, the release of DOX from DOX-SWCNHs and DOX-O-SWCNHs was almost similar, thereby showing insignificant difference at the pH values of 5.5 and 7.4 [42]. The drug also presented remarkable pH-dependent drug release from IL-21-PSL-DOX-O-SWCNHs, thereby showing a higher release rate at the pH of 5.5 than at 7.4. The DOX release from IL-21-PSL-DOX-O-SWCNHs was lower than that of DOX-O-SWCNHs at the pH of 7.4. However, DOX release was similar to that of DOX-O-SWCNHs at the pH of 5.5. This result may be caused by the pH-responsive shell structure of IL-21 PSL, which easily disintegrated at acidic conditions, such as at the pH of 5.5 (Fig. 4B). As shown in Fig. 4A, the in vitro release of IL-21 from IL-21-PSL-DOX-O-SWCNHs at pH 5.5 was significantly faster than that at pH 7.4, thereby indicating that the disintegration of shell structure of IL-21-PSL-DOX-O-SWCNHs facilitated the release of IL-21 at the acidic pH. This result further suggested that IL-21 can be efficiently released in tumor microenvironment [43,44].

3.5. Cytotoxicity

The cytotoxicity of carriers on 293T and A549 cells was evaluated using WST-1 method. As shown in Fig. 5, different SWCNH, O-SWCNH, and PSL-O-SWCNH concentrations had unremarkable inhibition on the growth of A549 and 293T cells, thereby showing over 80% of cell viability at a concentration range from 3.125 to 100 μg/mL. The cell viability of drug-loaded SWCNHs on A549 cells was evaluated, and the IC$_{50}$ value was 164.85 μg/mL (Fig. 6). This result confirmed that carrier did not affect the cancer cell growth and cytotoxicity against noncancerous cells.

3.6. Cellular uptake and localization

Flow cytometry was used to quantify DOX uptake by A549 cells from DOX-O-SWCNHs and PSL-C6-DOX-O-SWCNHs. As shown in Fig. 7A and B, the cellular DOX level for DOX-O-SWCNHs and PSL-C6-DOX-O-SWCNHs was almost identical, thereby reaching up to 100%.

To investigate the cellular localization of nanocarriers further, IL-21 was replaced by a green fluorescence dye (coumarin-6) to obtain PSL-C6-DOX-O-SWCNHs. Then, fluorescence signals produced by C6 and DOX were observed for the subcellular locations of PSL-C6, DOX-O-SWCNHs, and PSL-C6-DOX-O-SWCNHs in A549 cells. As shown in the confocal images in Fig. 7C, the blue fluorescence of C6 from PSL-C6 and the red fluorescence of DOX from DOX-O-SWCNHs were almost wholly located in the cell. Meanwhile, blue and red fluorescence were observed in the cell when treated with PSL-C6-DOX-O-SWCNHs, thereby indicating that core-shell structure had no effect on nanocarrier internalization by A549 cells.

3.7. Macrophage polarization

3.7.1. Macrophage induction

In general, LPS and IL-4 differentiate RAW 264.7 cells into M1 and M2 phenotypes, respectively [45]. We analyzed the markers of M1 (iNOs and IL-12) or M2 (IL-10 and TGF-β) type macrophage by using qPCR after treatment with LPS and IL-4. After treatment with LPS for 24 h, IL-12 and iNOs levels were significantly upregulated, whereas the IL-10 level was significantly downregulated. However, the TGF-β level showed insignificant change. By contrast, after treatment with IL-4 for 24 h, IL-12, and iNOs levels were significantly up-regulated, whereas iNOs level was significantly down-regulated. However, IL-12 expression showed insignificant increase (Fig. 8). Hence, iNOs and IL-10 are the potential markers in evaluating M1 and M2 type macrophages in this study.

The immunoregulatory activities of LPS at different concentrations in macrophages were assessed by checking the mRNA levels of iNOs and IL-10. As shown in Fig. S3, in a concentration-dependent manner, LPS upregulated the mRNA expression of iNOs. However, the mRNA expression of IL-10 was downregulated as the LPS concentration increased. The activities of different IL-4 concentrations on macrophage differentiation were also evaluated by detecting the mRNA levels of iNOs and IL-10. As shown in Fig. S4, iNOs expression was significantly downregulated by IL-4 at a concentration range of 6.25–100 ng/mL, but the maximum upregulation of IL-10 appeared at a concentration of 12.5 ng/mL.

3.7.2. IL-21 shifting macrophages from M2 to M1

To determine if the cytokine IL-21 was potent enough to convert one polarized macrophage phenotype to the opposing phenotype, we set up a two-stage polarization program. First, macrophages were treated with IL-4 for 24 h to induce their conversion into M1 and then treated with different IL-21 concentrations directly for 24 h. When cells were first cultured with IL-4, they showed low iNOs expression. However, when the medium was switched to IL-21, IL-10 expression was downregulated, and iNOs expression was upregulated (Fig. 9)

3.7.3. IL-21-PSL-O-SWCNHs shifting macrophages from M2 to M1

Polarization converting factor IL-21-loaded nanocarriers were also evaluated for shifting macrophages from M2 to M1. When TAMs were treated with IL-21-PSL-O-SWCNHs, M1-type gene iNOs tended to be significantly upregulated, whereas M2-type gene IL-10 was significantly downregulated (Fig. 10). This demonstrated that IL-21 treatment to tumor site modulated TAM polarization, from the immune-suppressive phenotype (M2) to the immune-stimulatory phenotype (M1).

3.8. Tumor-targeting ability

Cy5.5-IL-21-PSL-DOX-O-SWCNHs, in which Cy5.5 was used as the fluorescence marker, were prepared to evaluate the active-targeting property of nanocarriers. The tumor accumulation and tissue distribution in tumor-bearing mice were detected using a small animal imaging equipment. After the intravenous injections of Cy5.5-IL-21 and Cy5.5-IL-21-PSL-DOX-O-SWCNHs, the fluorescence images at 0, 12, 24, and 48 h are shown in Fig. 11A. A remarkable fluorescent signal can be detected at the tumor site at 12 h for Cy5.5-IL-21-PSL-DOX-O-SWCNHs but not for Cy5.5-IL-21. Fig. 11B and C present the images of various organs at 48 h after treated with Cy5.5-IL-21 and IL-21-PSL-DOX-O-SWCNHs. Cy5.5-IL-21-PSL-DOX-O-SWCNHs exhibited enhanced tumor accumulations compared with Cy5.5-IL-21 while they were widely distributed in the liver and spleen. The significant tumor accumulation of Cy5.5-IL-21-PSL-DOX-O-SWCNHs indicated the excellent tumor targeting abilities of nanocarriers through the EPR effect [46].

3.9. In vivo antitumor effects

Fig. 12A and B show the tumor size and body weight changes of mice when treated with various nanocarriers. A remarkable change in tumor appearance appeared for the IL-21-PSL-DOX-O-SWCNH group compared with control the group (Fig. 12A). The body weight change for all treated groups was insignificant (Fig. 12B).

The antitumor efficacy of IL-21-PSL-DOX-O-SWCNHs was evaluated in A549 tumor-bearing mice. The changes in tumor volumes were detected continuously for 10 days during the treatment period. IL-21-PSL and PSL-DOX-O-SWCNHs slightly inhibited the tumor growth compared with the control group as shown in Fig. 12C. However, IL-21-PSL-DOX-O-SWCNHs showed more significant inhibition of the tumor growth than PSL-DOX-O-SWCNHs and IL-21-PSL. After 10 days of treatment, the tumor sizes of other treatment groups were much bigger than those of IL-21-PSL-DOX-O-SWCNHs group as shown in Fig. 12D. The powerful antitumor ability of IL-21-PSL-DOX-O-SWCNHs may be due to the synergistic effects of IL-21 and DOX induced by combining immunotherapy and chemotherapy [47].

4. Conclusions

A novel core–shell structure of SWCNHs and PSL was constructed for DOX and TAM polarization factor IL-21 (IL-21-PSL-DOX-O-SWCNH) codelivery. The release rates of IL-21 and DOX from nanocarriers at the pH of 7.4 was lower than those at the pH of 5.5, thereby indicating a pH-sensitive drug release. The IL-21-PSL-DOX-O-SWCNHs can be easily uptaken by A549 cells and significantly downregulate the M2 macrophage-related factor (IL-10) expression and upregulate that of M1 macrophage-related factors (iNOs). IL-21-PSL-DOX-O-SWCNH also showed remarkably high tumor-targeting and distribution and can significantly reduce the tumor volume of A549 lung cancer cells, thereby showing synergistic effects of DOX and IL-21. The novel functionalized IL-21-PSL-DOX-O-SWCNHs showed high drug loading, excellent cellular uptake, pH-sensitive release, polarization effect, and remarkable antitumor efficacy.

Author statement

Xiao-Xue Zhang: Conceptualization, Methodology, Formal analysis, Investigation, Writing – original draft. Ge Tong: Methodology, Formal analysis, Investigation. Dan Shen: Methodology, Formal analysis, Investigation. Xue-Cheng Li: Validation, Formal analysis. Li-Jing Lan: Validation, Formal analysis. Xin Liu: Validation, Formal analysis. Jing-Hao Cui: Writing – review & editing. Renyu Huang: Statistic analysis, Writing – review & editing. Beom-Jin Lee: Writing – review & editing. Hong Gao: Methodology, Formal analysis, Investigation. Qing-Ri Cao: Project administration, Resources, Writing – review & editing, Supervision, Funding acquisition.

Declaration of competing interest

The authors declare no conflict of interest.

Data availability

No data was used for the research described in the article.

Acknowledgments

Appendix A. Supplementary data

Supplementary data to this article can be found online at https://doi.org/10.1016/j.jddst.2023.104743.

References

[1] F. Bray, J. Ferlay, I. Soerjomataram, R.L. Siegel, L.A. Torre, A. Jemal, Global cancer statistics 2018: GLOBOCAN estimates of incidence and mortality worldwide for 36 cancers in 185 countries, Ca - Cancer J. Clin. 68 (6) (2018) 394–424.

[2] M. Sohail, W. Guo, Z.Y. Li, H. Xu, F. Zhao, D.Q. Chen, F.H. Fu, Nanocarrier-based drug delivery system for cancer therapeutics: a review of the last decade, Curr. Med. Chem. 28 (2021) 3753–3772.

[3] W.L. Chen, S.D. Yang, F. Li, J.Z. Li, Z.Q. Yuan, W.J. Zhu, Y. Liu, X.F. Zhou, C. Liu, X.N. Zhang, Tumor microenvironment-responsive micelles for pinpointed intracellular release of active ingredient and enhanced anti-cancer efficiency, Int. J. Pharm. 511 (2) (2016) 728–740.

[4] E. Frei, G.P. Canellos, Dose: a critical factor in cancer chemotherapy, Am. J. Med. 69 (4) (1980) 585–594.

[5] W.H. Redd, G.H. Montgomery, K.N. DuHamel, Behavioral intervention for cancer treatment side effects, J. Natl. Cancer Inst. 93 (11) (2001) 810–823.

[6] J.A. Kemp, M.S. Shim, C.Y. Heo, Y.J. Kwon, 'Combo' nanomedicine: Co-delivery of multi-modal therapeutics for efficient, targeted, and safe cancer therapy, Adv. Drug Deliv. Rev. 98 (2016) 3–18.

[7] T. May, D.P. Goldstein, R.S. Berkowitz, Current chemotherapeutic management of patients with gestational trophoblastic neoplasia, Chemother Res Pract (2011), 806256.

[8] D.E. Gerber, J.H. Schiller, Maintenance chemotherapy for advanced non-small-cell lung cancer: new life for an old idea, J. Clin. Oncol. 31 (8) (2013) 1009–1020.

[9] I. Akiko, M. Ruslan, Control of adaptive immunity by the innate immune system, Nat. Immunol. 16 (4) (2015) 343–353.

[10] R.S. Kerbel, B.A. Kamen, The anti-angiogenic basis of metronomic chemotherapy, Nat. Rev. Cancer 4 (6) (2004) 423–436.

[11] T. Kawai, S. Akira, Toll-like receptors and their crosstalk with other innate receptors in infection and immunity, Immunity 34 (5) (2011) 637–650.

[12] J.J. Wu, D.J. Waxman, Immunogenic chemotherapy: dose and schedule dependence and combination with immunotherapy, Cancer Lett. 419 (2018) 210–221.

[13] M. Vanneman, G. Dranoff, Combining immunotherapy and targeted therapies in cancer treatment, Nat. Rev. Cancer 12 (4) (2012) 237–251.

[14] I. Cheong, X. Huang, C. Bettegowda, L.A. Diaz Jr., K.W. Kinzler, S.B. Zhou, B. Vogelstein, A bacterial protein enhances the release and efficacy of liposomal cancer drugs, Science 314 (5803) (2006) 1308–1311.

[15] P. Gotwals, S. Cameron, D. Cipolletta, V. Cremasco, A. Crystal, B. Hewes, S. Quaratino, C. Sabatos-Peyton, L. Petruzzelli, J.A. Engelman, G. Dranoff, Prospects for combining targeted and conventional cancer therapy with immunotherapy, Nat. Rev. Cancer 17 (5) (2017) 286–301, 2017.

[16] Y. Cao, H.Y. Huang, L.Q. Chen, H.H. Du, J.H. Cui, L.W. Zhang, B.J. Lee, Q.R. Cao, Enhanced lysosomal escape of pH-responsive polyethylenimine-betaine functionalized carbon nanotube for the codelivery of survivin small interfering RNA and active ingredient, ACS Appl. Mater. Interfaces 11 (10) (2019) 9763–9776.

[17] T. Tan, L. Coussens, Humoral immunity, inflammation and cancer, Curr. Opin. Immunol. 19 (2) (2007) 209–216.

[18] T.A. Wynn, A. Chawla, J.W. Pollard, Macrophage biology in development, homeostasis and disease, Nature 496 (7446) (2013) 445–455.

[19] D.M. Mosser, J.P. Edwards, Exploring the full spectrum of macrophage activation, Nat. Rev. Immunol. 8 (12) (2008) 958–969.

[20] V.W. Ho, L.M. Sly, Derivation and characterization of murine alternatively activated (M2) macrophages, Methods Mol. Biol. 531 (2009) 173–185.

[21] M. Xu, M.Y. Liu, X.X. Du, S.R. Li, Intratumoral delivery of IL-21 overcomes anti-Her2/Neu resistance through shifting tumor-associated macrophages from M2 to M1 phenotype, J. Immunol. 194 (10) (2015) 4997–5006.

[22] S.K. Biswas, A. Mantovani, Macrophage plasticity and interaction with lymphocyte subsets: cancer as a paradigm, Nat. Immunol. 11 (10) (2010) 889–896.

[23] S. Iijima, M. Yudasaka, R. Yamada, S. Bandow, K. Suenaga, F. Kokai, K. Takahashi, Nano-aggregates of single-walled graphitic carbon nano-horns, Chem. Phys. Lett. 309 (1999) 165–170.

[24] N. Karousis, I. Suarez-Martinez, C.P. Ewels, N. Tagmatarchis, Structure, properties, functionalization, and applications of carbon nanohorns, Chem. Rev. 116 (8) (2016) 4850–4883.

[25] B. Li, X.X. Zhang, H.Y. Huang, L.Q. Chen, J.H. Cui, Y. Liu, H. Jin, B.J. Lee, Q.R. Cao, RGD-decorated chitosan-functionalized single-walled carbon nanotubes loading active ingredient effectively deactivate the A549 tumor cells in vitro and in vivo, Int. J. Pharm. 543 (1–2) (2018) 8–20.

[26] Z.Q. Yuan, W.L. Chen, B.G. You, Y. Liu, S.D. Yang, J.Z. Li, W.J. Zhu, X.F. Zhou, C. Liu, X.N. Zhang, Multifunctional nanoparticles co-delivering EZH2 siRNA and active ingredient for synergy therapy of orthotopic non-small-cell lung tumor, J. Contr. Release 268 (2017) 198–211.

[27] J. Chen, B.W. Yao, C. Li, G.Q. Shi, An improved Hummers method for eco-friendly synthesis of graphene oxide, Carbon 64 (2013) 225–229.

[28] M.T. Martinez, M.A. Callejas, A.M. Benito, M. Cochet, T. Seeger, A. Schreiber, J. Ansón, C. Gordon, C. Marhic, O. Chauvet, W.K. Maser, Modifications of single-wall carbon nanotubes upon oxidative purification treatments, Nanotechnology 14 (2003) 691–695.

[29] L. Fedele, L. Colla, S. Bobbo, S. Barison, F. Agresti, Experimental stability analysis of different water-based nanofluids, Nanoscale Res. Lett. 6 (1) (2011) 300.

[30] T. Zhang, T. Oyama, S. Horikoshi, J. Zhao, N. Serpone, H. Hidaka, Photocatalytic decomposition of the sodium dodecylbenzene sulfonate surfactant in aqueous titania suspensions exposed to highly concentrated solar radiation and effects of additives, Appl. Catal. B Environ. 42 (1) (2003) 13–24.

[31] E.S. Lee, K. Na, Y.H. Bae, Active ingredient loaded pH-sensitive polymeric micelles for reversal of resistant MCF-7 tumor, J. Contr. Release 103 (2) (2005) 405–418.

[32] J. Connor, L. Huang, pH-sensitive immunoliposomes as an efficient and target-specific carrier for antitumor drugs, Cancer Res. 46 (7) (1986) 3431–3435.

[33] M. Li, Z. Tang, S. Lv, W. Song, H. Hong, X. Jing, Y. Zhang, X. Chen, Active Ingredient crosslinked pH-sensitive nanoparticles for efficient delivery of active ingredient, Biomaterials 35 (12) (2014) 3851–3864.

[34] Y.J. Gu, J. Cheng, J. Jin, S.H. Cheng, W.T. Wong, Development and evaluation of pH-responsive single-walled carbon nanotube-active ingredient complexes in cancer cells, Int. J. Nanomed. 6 (2011) 2889–2898.

[35] H. Ellens, J. Bentz, F.C. Szoka, pH-induced destabilization of phosphatidylethanolamine-containing liposomes: role of bilayer contact, Biochemistry 23 (7) (1984) 1532–1538.

[36] K. Sato, K. Yoshida, S. Takahashi, J.I. Anzai, pH-and sugar-sensitive layer-by-layer films and microcapsules for drug delivery, Adv. Drug Deliv. Rev. 63 (9) (2011) 809–821.

[37] S. Zhu, X.E. Zhao, J. You, G. Xu, H. Wang, Carboxylic-group-functionalized single-walled carbon nanohorns as peroxidase mimetics and their application to glucose detection, Analyst 140 (18) (2015) 6398–6403.

[38] F. Wang, Y.C. Wang, S. Dou, M.H. Xiong, T.M. Sun, J. Wang, Active ingredient-tethered responsive gold nanoparticles facilitate intracellular drug delivery for overcoming multidrug resistance in cancer cells, ACS Nano 5 (5) (2011) 3679–3692.

[39] K.S. Oh, H. Lee, J.Y. Kim, E.J. Koo, E.H. Lee, J.H. Park, S.Y. Kim, K. Kim, I.C. Kwon, S.H. Yuk, The multilayer nanoparticles formed by layer by layer approach for cancertargeting therapy, J. Contr. Release 165 (1) (2013) 9–15.

[40] J. Fan, M. Yudasaka, J. Miyawaki, K. Ajima, K. Murata, S. Iijima, Control of hole opening in single-wall carbon nanotubes and single-wall carbon nanohorns using oxygen, J. Phys. Chem. B 110 (4) (2006) 1587–1591.

[41] M. Yudasaka, M. Zhang, S. Iijima, Diameter-selective removal of single-wall carbon nanotubes through light-assisted oxidation, Chem. Phys. Lett. 374 (2003) 132–136.

[42] C. Wang, X. Wang, T. Zhong, Y. Zhao, W.Q. Zhang, W. Ren, D. Huang, S. Zhang, Y. Guo, X. Yao, Y.Q. Tang, X. Zhang, Q. Zhang, The antitumor activity of tumor-homing peptide-modified thermosensitive liposomes containing active ingredient on MCF-7/ADR: in vitro and in vivo, Int. J. Nanomed. 10 (2015) 2229–2248.

[43] B.X. Zhao, Y. Zhao, Y. Huang, L.M. Luo, P. Song, X. Wang, S. Chen, K. Yu, X. Zhang, Q. Zhang, The efficiency of tumor-specific pH-responsive peptide-modified polymeric micelles containing active ingredient, Biomaterials 33 (8) (2012) 2508–2520.

[44] S.R. Paliwal, R. Paliwal, S.P. Vyas, A review of mechanistic insight and application of pH-sensitive liposomes in drug delivery, Drug Deliv. 22 (3) (2015) 231–242.

[45] L. Chavez-Galan, M.L. Olleros, D. Vesin, I. Garcia, Much more than M1 and M2 macrophages, there are also CD169(+) and TCR(+) macrophages, Front. Immunol. 6 (2015) 263.

[46] G. Wang, M. Tschoi, R. Spolski, Y. Lou, K. Ozaki, C. Feng, G. Kim, W.J. Leonard, P. Hwu, In vivo antitumor activity of interleukin 21 mediated by natural killer cells, Cancer Res. 63 (2003) 9016–9022.

[47] C. Rolny, M. Mazzone, S. Tugues, D. Laoui, I. Johansson, C. Coulon, M.L. Squadrito, I. Segura, X. Li, E. Knevels, HRG inhibits tumor growth and metastasis by inducing macrophage polarization and vessel normalization through downregulation of PlGF, Cancer Cell 19 (1) (2011) 31–44.